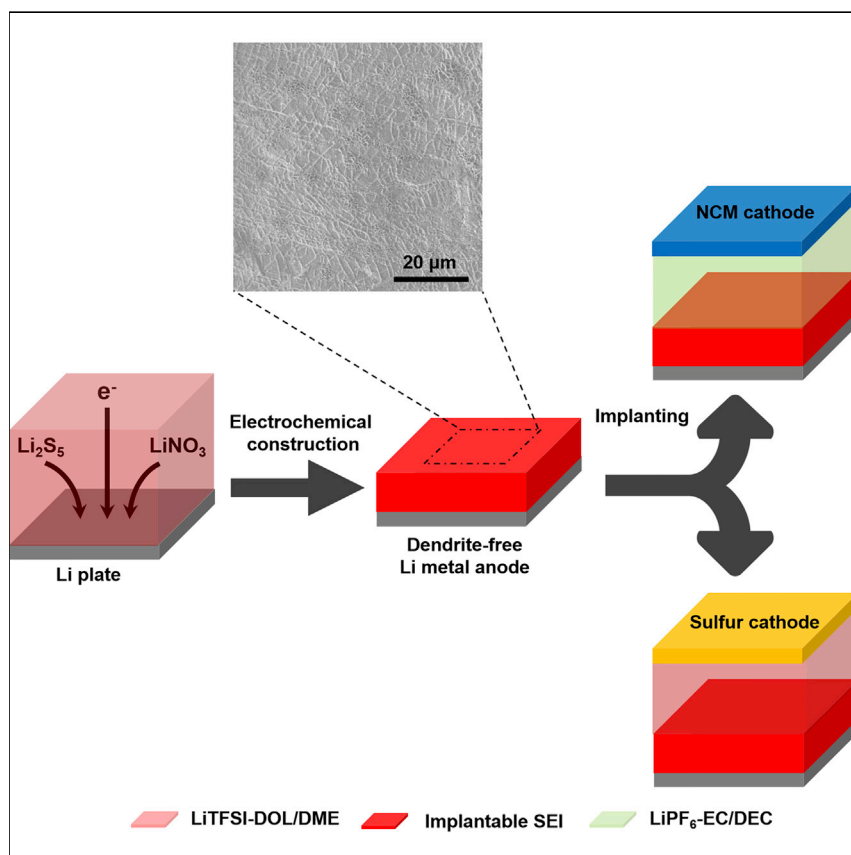


## Article

# Implantable Solid Electrolyte Interphase in Lithium-Metal Batteries



Lithium (Li) metal is regarded as the “Holy Grail” electrode because of its low electrochemical potential and high theoretical capacity. Unfortunately, uncontrolled dendritic Li growth induces low efficiency and poor safety. Here, we propose an electrochemical strategy for constructing an ultra-stable implantable solid electrolyte interphase (SEI) on Li metal. The SEI rendered dendrite-free Li deposits in a working battery. Li metal with a stable SEI can be transplanted into ether and ester electrolytes to efficiently cycle sulfur and  $\text{LiNi}_{0.5}\text{Co}_{0.2}\text{Mn}_{0.3}\text{O}_2$  cathodes, respectively.

Xin-Bing Cheng, Chong Yan,  
Xiang Chen, ..., Rui Zhang,  
Shu-Ting Yang, Qiang Zhang

zhang-qiang@mails.tsinghua.edu.cn

## HIGHLIGHTS

An ultra-stable implantable SEI was constructed by the electroplating method

The implantable SEI, with a dual-layer structure, can suppress Li dendrite growth

Li-metal anode with implantable SEI works well in ether and ester electrolytes

Li-metal anode with implantable SEI cycles sulfur and oxide cathodes well



Cheng et al., Chem 2, 258–270  
February 9, 2017 © 2017 Elsevier Inc.  
<http://dx.doi.org/10.1016/j.chempr.2017.01.003>

## Article

# Implantable Solid Electrolyte Interphase in Lithium-Metal Batteries

Xin-Bing Cheng,<sup>1,3</sup> Chong Yan,<sup>1,2,3</sup> Xiang Chen,<sup>1</sup> Chao Guan,<sup>1</sup> Jia-Qi Huang,<sup>1</sup> Hong-Jie Peng,<sup>1</sup> Rui Zhang,<sup>1</sup> Shu-Ting Yang,<sup>2</sup> and Qiang Zhang<sup>1,4,\*</sup>

## SUMMARY

Lithium (Li) metal is regarded as the “Holy Grail” electrode because of its low electrochemical potential and high theoretical capacity. Unfortunately, uncontrolled dendritic Li growth induces low coulombic efficiency and poor safety during deposition. Here, we propose an *ex situ* electrochemical strategy for constructing an ultra-stable implantable solid electrolyte interphase (SEI) on a Li-metal anode. In our study, the SEI rendered dendrite-free Li deposits in a working battery. A Li-metal anode with a stable SEI can be transplanted into ether and ester electrolyte to cycle sulfur (S) and a  $\text{LiNi}_{0.5}\text{Co}_{0.2}\text{Mn}_{0.3}\text{O}_2$  (NCM) cathode, respectively. The Li-S cell exhibited superb long-term cycling performance at 1.0 C with an initial capacity of  $890 \text{ mAh g}^{-1}$  and capacity retention of 76% after 600 cycles. When matching the NCM cathode, the Li-metal anode with an implantable SEI avoided activation and increased capacity by 50% from 100 to  $150 \text{ mAh g}^{-1}$ . A Li-metal anode with implantable SEI protection delivers new insights into the rational design of Li-metal batteries with many alternative cathodes and electrolyte systems.

## INTRODUCTION

Portable devices (including smartphones and laptops) are changing our lifestyles, resulting in an everlasting thirst for higher-energy batteries. Compared with the explosion of chip technology, whose memory capacity has doubled every 2 years, the advances in rechargeable batteries have seriously lagged behind with an average increase of only 8%–9% per year.<sup>1</sup> Tremendous progress in energy chemistry and advanced materials has led to energy storage devices with high energy density, long lifespans, and enhanced safety.<sup>2,3</sup> Lithium (Li) metal has been regarded as the “Holy Grail” electrode because of its low electrode potential ( $-3.040 \text{ V}$  versus standard hydrogen electrode) and high capacity ( $3,860 \text{ mAh g}^{-1}$ ) and is thus under extensive investigation. Consequently, Li-metal batteries (LMBs) are considered promising next-generation energy storage systems.<sup>4–8</sup> The uncontrolled growth of Li dendrites, however, leads to the dilemma of fluctuating coulombic efficiency and formidable safety issues, unfortunately terminating the commercialization of LMBs.

Most commercial LIBs and next-generation LMBs, including Li-sulfur (Li-S) and Li-oxygen batteries and batteries with Li-rich layered cathode and Li-metal anode, generally use non-aqueous liquid electrolytes.<sup>9,10</sup> An electrically insulating but ionically conductive film is formed on the anode surface through spontaneous reactions between electrolytes and Li metal during the initial charging cycles.<sup>7</sup> An ideal solid electrolyte interphase (SEI) would be expected to suppress dendritic growth of Li metal if several desired properties, such as robust chemical stability, extraordinary

## The Bigger Picture

Li-ion batteries (LIBs) with a graphite anode have achieved great success in portable devices and electronic vehicles. Nevertheless, LIBs cannot satisfy the ever-increasing demand for electrified products. Because it addresses the issue of duration, Li metal is regarded as the “Holy Grail” of electrodes. Li-metal batteries have been forecasted to be a bright prospect for energy storage devices, although Li anodes are burdened by safety concerns and low utilization induced by dendrite growth. Here, we proposed suppressing Li dendrite growth by constructing an implantable solid electrolyte interphase (SEI). This SEI can effectively suppress dendrite growth and works well in Li-S and Li- $\text{LiNi}_{0.5}\text{Co}_{0.2}\text{Mn}_{0.3}\text{O}_2$  batteries with ether and ester electrolytes, respectively. If this electroplating strategy can be adopted for coating commercial Li-metal electrodes, the dendrite issue is expected to be conveniently and effectively handled, which will generate sustainable development in the battery industry.

Li-ion ( $\text{Li}^+$ ) conductivity, and high modulus, could be afforded simultaneously. Practical SEIs in working cells, however, always exhibit poor stability, dynamic geometric and compositional variations, low  $\text{Li}^+$  conductivity, and moderate modulus.<sup>11</sup> The huge volume fluctuation of Li upon cycling results in undesirable mechanical cracks in the SEI. The energy boundary and strong electric field near these cracks induce prioritized nucleation and rapid deposition.<sup>12</sup> Consequently, SEIs in practical cells cannot effectively protect the Li-metal anode to suppress dendrite growth.

Several strategies have been proposed for constructing a stable and efficient SEI to suppress the growth of Li dendrites. Zu et al. used a copper acetate additive to significantly reduce the crystallinity of the SEI and stabilize the Li-metal anode.<sup>13</sup> Li halides, especially LiF, lower the diffusing energy of Li ions, have high surface energy, and hence exhibit an overwhelming advantage in enhancing the surface diffusion of  $\text{Li}^+$  during electrodeposition and directing a dendrite-free morphology.<sup>14,15</sup> A nanostructured electrolyte can efficiently suppress Li dendrite growth by fixing the anions spatially to modify the local distribution of the electrical field.<sup>16–18</sup> High-salt-concentration electrolytes, in which the Li-metal anode is stabilized by a great reduction in the number of free solvent molecules,<sup>19,20</sup> have also emerged.<sup>21,22</sup> Other modifications to electrolytes (including  $\text{Cs}^+$ <sup>23</sup> and fluoroethylene carbonate<sup>24</sup>) and the rational design of nanostructured electrodes (including Li-metal microspheres,<sup>25</sup> Li metal confined in graphene,<sup>26–28</sup>  $\text{Li}_7\text{B}_6$  matrix,<sup>29</sup> 3D current collectors,<sup>30–32</sup> hybrid anode structure,<sup>33</sup> polar surface modification,<sup>34,35</sup> and encapsulation of Li through heterogeneous seed<sup>36</sup>) have also been proposed to suppress Li dendrite growth. Nevertheless, these methods are always restricted to a specific cathode or electrolyte system. Few approaches have been efficiently implemented in various LMB systems as a result of their complexity or incompatibility with a certain positive electrode (or electrolyte). Therefore, exploring facile and versatile strategies toward high-efficiency, dendrite-free, and safe Li-metal anodes is still challenging.

In this article, we present a facile, versatile, and tunable approach to Li-metal anodes whereby an implantable SEI is generated via a general electroplating method involving precycling Li metal in a Li bis-trifluoromethanesulfonimide (LiTFSI, 1.0 M)- $\text{LiNO}_3$  (5.0 wt %)- $\text{Li}_2\text{S}_5$  (0.02 M)-1,3-dioxolane (DOL)/1,2-dimethoxyethane (DME) ternary salt electrolyte. Compared with other ex situ (or artificial) SEIs (such as hollow carbon nanospheres,<sup>37</sup>  $\text{Li}_3\text{PO}_4$ <sup>38</sup>), the implantable SEI is an actual SEI formed in situ on the Li-metal anode from a working cell. Because of the complexity of the structure and composition of real SEIs in working cells,<sup>11</sup> a coating layer of only one material cannot satisfy the demand for a real SEI film and act as an inherently self-adaptive protective layer on a Li-metal anode for various systems. An implantable SEI is expected to protect Li metal synergistically and adaptively. A Li-metal anode with the protection of an as-obtained SEI can efficiently match both sulfur and  $\text{LiNi}_{0.5}\text{Co}_{0.2}\text{Mn}_{0.3}\text{O}_2$  (NCM) cathodes and enhance the performance ubiquitously. Note that this strategy is not limited to LiTFSI- $\text{LiNO}_3$ - $\text{Li}_2\text{S}_5$  ternary salts. This strategy will generate tremendous opportunities in the search for novel SEI initiators for emerging LMBs.

## RESULTS

### Electrochemical Construction of SEI on Li Metal

We obtained the electroplated implantable SEI by precycling Li metal in a LiTFSI- $\text{LiNO}_3$ - $\text{Li}_2\text{S}_5$  ternary salt electrolyte (Figure 1A). Compared with other species and concentrations of Li polysulfides (LiPSs,  $\text{Li}_2\text{S}_x$ ,  $x = 1-8$ ), 0.02 M  $\text{Li}_2\text{S}_5$  in an ether electrolyte has the benefit of forming a stable SEI to stabilize a Li-metal anode when combined with  $\text{LiNO}_3$  and LiTFSI synergistically.<sup>39</sup> The as-obtained SEI was very dense and flat and

<sup>1</sup>Beijing Key Laboratory of Green Chemical Reaction Engineering and Technology, Department of Chemical Engineering, Tsinghua University, Beijing 100084, China

<sup>2</sup>National & Local Joint Engineering Laboratory for Motive Power and Key Materials, College of Chemistry and Chemical Engineering, Henan Normal University, Xinxiang 453007, China

<sup>3</sup>Co-first author

<sup>4</sup>Lead Contact

\*Correspondence:  
zhang-qiang@mails.tsinghua.edu.cn  
<http://dx.doi.org/10.1016/j.chempr.2017.01.003>

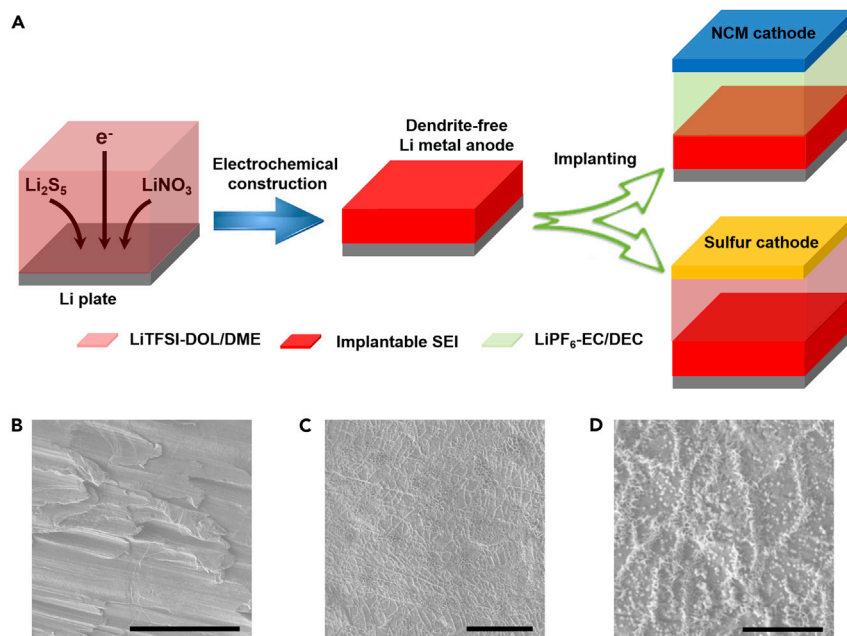


**Figure 1. Schematic of Ex Situ SEI Construction and Morphology of the Induced Li Plate**

(A) Ex situ SEI construction on the Li plate by electrochemical methods in 1.0 M LiTFSI-DOL/DME electrolyte with 0.020 M  $\text{Li}_2\text{S}_5$ -5.0 wt %  $\text{LiNO}_3$  hybrid additives and its applications in Li-S and Li-NCM batteries.

(B–D) Scanning electron microscopy (SEM) images of (B) a pristine Li plate and (C and D) a Li plate with SEI coating layer (D is an enlarged view of C). The scale bars represent 100  $\mu\text{m}$  (B), 20  $\mu\text{m}$  (C), and 4  $\mu\text{m}$  (D).

could bear the plating and stripping of Li ions on the Li-metal anode. In most cases, a commercial Li metal (referred to as the COM electrode, Figure 1B) contains many protruberances of several micrometers, which can be nucleation sites for dendritic crystals and lead to dendrite growth.<sup>34</sup> After being precycled in ternary salt electrolyte, the routine Li metal was encapsulated by a uniform and multifunctional mosaic layer (advanced electrode, Figures 1C and 1D). The advanced Li-metal anode displayed a smooth surface morphology and well-organized skeleton, which served as smooth depositing sites for dendrite-free Li deposition.

### Surface Chemistry of Electroplated SEI

According to the X-ray photoelectron spectroscopy (XPS) results (Figure S1), the SEI formed in the LiTFSI- $\text{LiNO}_3$ - $\text{Li}_2\text{S}_5$  ternary salt electrolyte includes organic composites of  $\text{ROCO}_2\text{Li}$  and  $\text{ROLi}$  and inorganic composites of  $\text{Li}_3\text{N}$ ,  $\text{Li}_2\text{N}_x\text{O}_y$ ,  $\text{LiF}$ ,  $\text{Li}_2\text{S}_x$ , and  $\text{Li}_2\text{S}_x\text{O}_y$ , which agrees well with previous publications.<sup>40,41</sup> The dense inorganic layer with appropriate proportions of  $\text{Li}_3\text{N}$ ,  $\text{Li}_2\text{N}_x\text{O}_y$ ,  $\text{LiF}$ ,  $\text{Li}_2\text{S}_x$ , and  $\text{Li}_2\text{S}_x\text{O}_y$  isolates electron transfer, desolvates Li ions to free ones, and promotes Li-ion diffusion. For example,  $\text{LiF}$  is believed to be a robust electronic insulator with poor ionic conductivity ( $\sim 10^{-31} \text{ S cm}^{-1}$ ),<sup>42</sup> whereas  $\text{Li}_2\text{S}_x$  and  $\text{Li}_2\text{S}_x\text{O}_y$  can considerably enhance the conductivity of Li ions. Consequently, neither component alone affords the desired properties for an ideal SEI. They benefit from each other when they coexist in the SEI, although the exact synergistic cooperation mechanism is unknown.<sup>11</sup> The mosaic multifunctional SEI delivers great potential to efficiently improve the discharge capacity and lifespan of LMBs.

Li metal with this electroplated SEI can be implanted in various electrochemical systems, such as Li-S and Li-NCM batteries (Figure 1A). As indicated by the theoretical

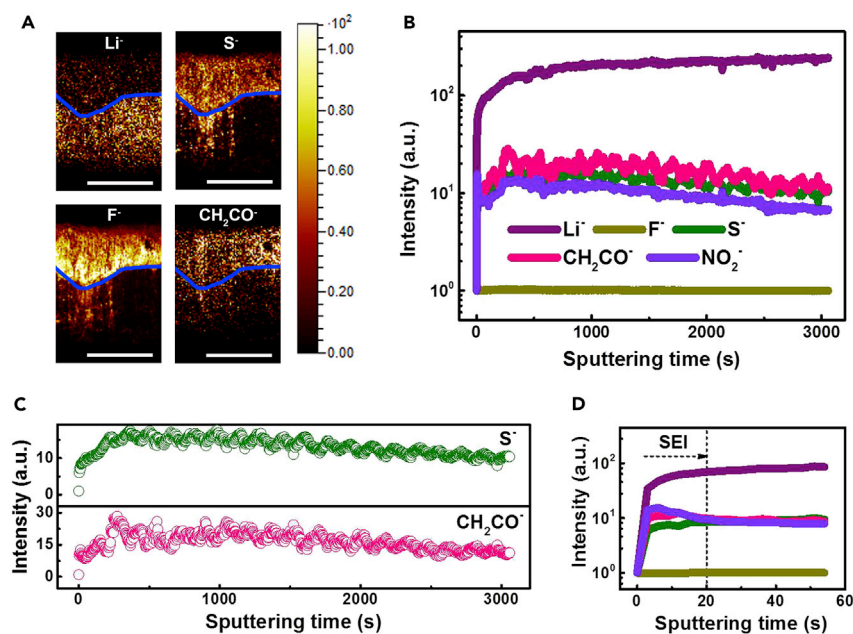


**Figure 2. Element Distribution in the Advanced Li-Metal Anode**

(A) TOF-SIMS chemical mapping to indicate the  $\text{Li}^+$ ,  $\text{S}^-$ ,  $\text{F}^-$ , and  $\text{CH}_2\text{CO}^-$  species in the protective SEI layer of the Li anode. The blue line was artificially created to show the boundary of the reactive and residual Li. Scale bars represent 200  $\mu\text{m}$ .

(B) TOF-SIMS depth profiles of  $\text{Li}^+$ ,  $\text{S}^-$ ,  $\text{F}^-$ , and  $\text{CH}_2\text{CO}^-$  species in the protective SEI layer on the Li anode. The intensities of all the species are normalized to the first signal obtained.

(C and D) Parts of the TOF-SIMS depth profiles to emphasize (C)  $\text{S}^-$  and  $\text{CH}_2\text{CO}^-$  species and (D) the sputtering time from 0 to 60 s.

calculations, the highest occupied molecular orbitals (HOMOs) of SEI components are lower than the lowest unoccupied molecular orbitals (LUMOs) of organic solvents (Figure S2). The HOMOs of solvents are lower than the LUMOs of SEI components. Therefore, the electroplated SEI is stable against DOL/DME and ethylene carbonate/diethyl carbonate (EC/DEC) solvents, guaranteeing successful operation of an advanced Li-metal anode when matched to sulfur and NCM cathodes.

We performed XPS to explore the surface chemistry of an advanced anode in a Li hexafluorophosphate ( $\text{LiPF}_6$ )-EC/DEC electrolyte, which is usually paired with a NCM cathode (Figure S3). After cycling in the EC/DEC electrolyte, the advanced and COM anodes exhibited similar C 1s species, but that of the advanced anode showed a sharp increase in the content of  $\text{Li}_2\text{CO}_3$  (Figure S3A).  $\text{LiF}$ , a critically important component to keep the SEI stable in the advanced electrode, can be well maintained and strengthened (Figure S3B). Although cycled in the electrolyte with non-S/N content, the advanced anode still preserved the content of  $\text{Li}_3\text{N}$  and  $\text{LiN}_x\text{O}_y$  in N 1s species and  $\text{Li}_2\text{S}$  and  $\text{LiS}_x\text{O}_y$  in S 2p species (Figures S3C and S3D). Consequently, after cycling in the EC/DEC electrolyte, the advanced anode still maintained excellent stability.

To further probe element depth distribution in the electroplated SEI, we performed time-of-flight secondary ion mass spectrometry (TOF-SIMS) cross-section mapping and depth profiling of the advanced Li metal (Figure 2). Here,  $\text{S}^-$  and  $\text{F}^-$  were chosen as the representative inorganic components, and  $\text{CH}_2\text{CO}^-$  species was chosen as the organic component. The cross-section mappings of  $\text{Li}^+$ ,  $\text{S}^-$ ,  $\text{F}^-$ , and  $\text{CH}_2\text{CO}^-$  species clearly illustrated a dual structure (reactive and residual Li) of the advanced

anode (Figure 2A), which is consistent with the reported literature.<sup>13</sup> Especially, the signal of F<sup>-</sup> species in reactive Li was much stronger than that in the residual Li, indicating that F<sup>-</sup> species (mainly LiF; Figure S3B) concentrate in reactive Li. LiF has been demonstrated to play a critically important role in constructing a stable and efficient SEI;<sup>14,21,24</sup> therefore, a SEI with a LiF-rich layer provides effective protection on Li metal.

To investigate the exact distribution of different species in a cross-section of the advanced Li-metal anode, we conducted 3,000 s Cs<sup>+</sup> sputtering (~2 μm) to obtain a depth profile (Figure 2B). With the increase in sputtering time, the signal of the Li<sup>-</sup> species went up, whereas signals of S<sup>-</sup> and CH<sub>2</sub>CO<sup>-</sup> species went down. The situation was quite different for F<sup>-</sup> species, which remained nearly stable throughout sputtering. The increase in Li<sup>-</sup> signal indicates that there are more organic Li-poor components in the SEI close to the electrolyte and more inorganic Li-rich elements in the SEI near Li metal. Furthermore, the intensity of S<sup>-</sup> showed a reverse fluctuant trend in relation to CH<sub>2</sub>CO<sup>-</sup> species (Figure 2C). When the concentration of S<sup>-</sup> species increased, that of CH<sub>2</sub>CO<sup>-</sup> species decreased. Given that S<sup>-</sup> and CH<sub>2</sub>CO<sup>-</sup> species represent the inorganic and organic components of the SEI, respectively, their opposite trends confirm the dual organic and inorganic structure of the SEI. On the top layer of the Li surface, whose thickness was estimated to be ~13.6 nm (t = 20 s and sputtering rate = 0.68 nm s<sup>-1</sup>), the amounts of Li<sup>-</sup>, S<sup>-</sup>, CH<sub>2</sub>CO<sup>-</sup>, and NO<sub>2</sub><sup>-</sup> tended to be relatively stable (Figure 2D). The thickness of the SEI layer was estimated to be 13.6 nm, which was also confirmed by transmission electron microscopy (TEM) (Figure S4).

### Dendrite-Inhibiting Behavior

Li-depositing behavior on the advanced and COM Li metals is shown in Figure 3. We conducted an aggressive test by allowing continuous deposition of Li ions onto Li metal until short circuit (15 mV is defined as the voltage for short circuit). From the voltage-time curves in Figures 3A and 3D, the COM and advanced cells indicate a short-circuit time of 3 and 5.5 hr, respectively. After deposition for 3 hr, the COM anode indicated an up-and-down surface morphology with a height difference of ~200 μm (Figures 3B and 3C). The uneven surface was mainly induced by large dendrite growth. On the contrary, the advanced anode had a faultlessly uniform surface without dendrites (Figures 3E and 3F). The increase in short-circuit time and dendrite-free Li deposition morphology of the advanced Li-metal anode clearly indicate its decisive role in suppressing Li dendrite growth and improving the safety performance of LMBs.

To clearly establish the behavior of Li deposition and the morphology of the advanced Li anode, we employed in situ optical microscopy to observe the cell with the advanced and COM Li anodes as symmetrical electrodes (Figure 3G). The electrodes were cycled at an ultra-high current density of 67 mA cm<sup>-2</sup>, and each deposition and stripping time was set to 100 s. Before Li deposition, the surface of the advanced and COM Li electrodes was smooth (Figure 3H). After 34 min (tenth Li deposition-stripping cycle), optically visible dendrites were observed on the COM anode, whereas the advanced anode surface was still smooth. After 42 min of cycling (12<sup>th</sup> Li deposition-stripping cycle), there were tiny dendrites on the advanced anode, whereas large dendrites nearly covered the surface of the COM anode. At 61 min (18<sup>th</sup> Li deposition-stripping cycle), dendrites on the COM and advanced electrodes met each other, resulting in cell short circuit. At the end, the volume of the COM electrode was nearly twice as large as that of the advanced electrode, indicating more Li dendrites on the surface of the COM electrode.

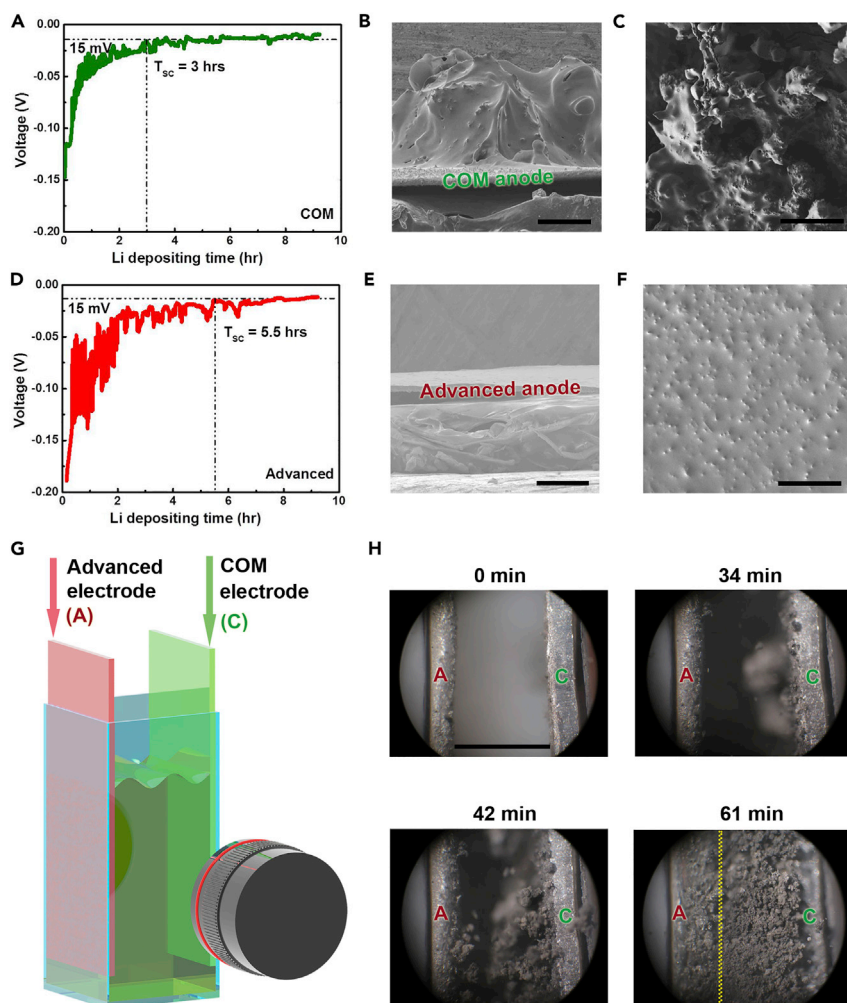


**Figure 3. Dendrite-Inhibiting Behavior of the Li-Metal Anode**

(A–F) Voltage–time curves for Li-ion continuous deposition onto (A) the COM electrode and (D) the advanced Li-metal anode at  $0.5 \text{ mA cm}^{-2}$ . Electrode morphology after 3 hr Li-ion deposition onto (B and C) the COM electrode and (E and F) the advanced electrode at  $0.5 \text{ mA cm}^{-2}$ . Both side views (B and E) and top views (C and F) are shown.

(G) Schematic of cells for in situ optical observation of Li dendrite growth on the surface of the COM and advanced electrodes at  $67 \text{ mA cm}^{-2}$  with charging and discharging times of 100 s.

(H) The cross-section morphology of the COM and advanced electrodes at an ultra-large current density of  $67 \text{ mA cm}^{-2}$ . The yellow line was artificially created to show the boundary of deposited Li in the cathode and anode.

The scale bars represent  $100 \mu\text{m}$  (B and E),  $60 \mu\text{m}$  (C and F), and  $0.7 \text{ cm}$  (distance between the COM and advanced electrodes in H).

### Proof of Concept of a Li Anode with an Implantable SEI in a Li-S Battery

Because of their very high theoretical energy density of  $2,600 \text{ Wh kg}^{-1}$ , Li-S batteries have been considered promising next-generation energy storage devices.<sup>43</sup> However, Li-S batteries with a Li-metal anode inevitably encounter Li dendrite issues. Even worse, LiPS intermediates can dissolve, diffuse, and react with Li metal, which makes the dendrite issue more complicated in a cell according to multi-electron conversion chemistry.

To settle the dendrite issues, we investigated the advanced Li metal with an implantable SEI as the anode of a Li-S battery. A Li-S cell with an advanced Li-metal anode

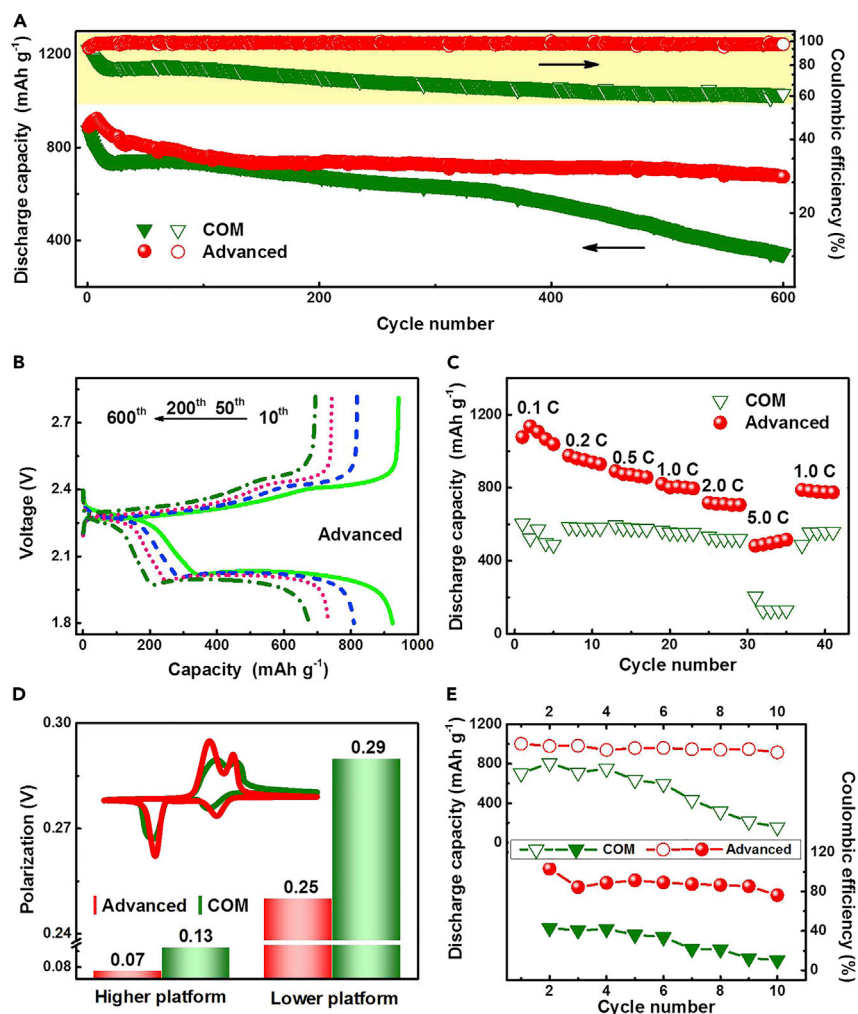


**Figure 4. Electrochemical Performance of Li-S Batteries with the Advanced Li-Metal Anode**

(A–D) Discharge capacity and coulombic efficiency at 1.0 C ( $1,675 \text{ mA g}^{-1}$ ) (A), charge and discharge curves (B), rate performance (C), and CV test (D) of Li-S coin cells.

(E) Discharge capacity and coulombic efficiency of Li-S pouch cells at 0.1 C.

(referred to as the advanced Li-S cell) exhibited a high initial discharge capacity of  $891 \text{ mAh g}^{-1}$  and a very large capacity retention rate of 76% after 600 cycles at 1.0 C ( $1.0 \text{ C} = 1,672 \text{ mA g}^{-1}$ ) (Figure 4A). This was much higher than that of a cell with a COM Li anode (referred to as the COM Li-S cell), which had a low retention of 39% after 600 cycles from an initial capacity of  $874 \text{ mAh g}^{-1}$ . The coulombic efficiency of the advanced cell in 600 cycles reached 98.6% without any additives, whereas that of the COM cell decayed sharply from 93% to 61%.

The advanced Li-S cell showed a distinct two-platform discharge with high and low platforms at 2.27 and 2.05 V, respectively (Figure 4B). After 150 cycles, the surface morphology of the Li-metal anode was tracked (Figure S5). Relative to the uneven surface and powdery Li deposits on the COM anode, the surface of the advanced Li anode was uniform, smooth, and dense. After 300 cycles, the cross-section morphology of the Li-metal anode was tracked (Figure S6). With the protection of a stable SEI, the advanced anode maintained a uniform morphology. However, more highly resistive reactive Li was present in the COM anode, and the SEI layer

became thicker. Consequently, a stable electroplated SEI can be implanted from a half-cell with  $\text{Li}_2\text{S}_5$ -containing electrolyte to a full Li-S cell with superior Li deposition behavior and high long-term cycling stability.

The advanced Li anode also had a superior rate performance (Figure 4C). When the current density was increased from 0.1 to 1.0 to 5.0 C, the discharge capacities of the advanced cell were 1,136, 822, and 521  $\text{mAh g}^{-1}$ , respectively, and those for the COM cells were 604, 553, and 130  $\text{mAh g}^{-1}$ , respectively. The low discharge capacity of the COM cells at low rates was induced by a severe LiPS shuttle. The significantly enhanced rate performance is ascribed to the reduced LiPS shuttle and lowered polarization, which were confirmed by cyclic voltammetry (CV) (Figure 4D). The high rate performance and low polarization of the CV test demonstrated the highly conductive nature of the electroplated SEI.

To probe the potential practical applications of advanced Li-metal anodes in Li-S batteries, we assembled pouch cells. Compared with the COM cell, the advanced cell showed an obvious improvement in the tenth discharge capacity (from 156 to 917  $\text{mAh g}^{-1}$ ) and coulombic efficiency (from 12% to 85%) at 0.1 C (Figure 4E). The multifunctional electroplated SEI effectively prevented the fresh Li from having direct contact with polysulfide anions, consequently inhibiting the interfacial reactions between polysulfides and Li metal and blocking the shuttle behavior of Li polysulfides.

#### Proof of Concept of a Li Anode with an Implantable SEI Matching the NCM Cathode

$\text{LiNi}_x\text{Co}_y\text{Mn}_z\text{O}_2$  ( $0 \leq x, y, z < 1$ ) is considered to be one of the most important cathode materials for next-generation battery energy storage systems because of its high theoretical capacity and cost effectiveness.<sup>44,45</sup> Here, we used an advanced Li-metal anode to match the NCM cathode to render a high-energy-density LMB. We used a high NCM loading of 12.02  $\text{mg cm}^{-2}$  to ensure that a significant portion of the Li metal from the anode was stripped and deposited during cell cycling. Thus, the cycling performance reflects the nature of the Li-metal anode rather than the cathode. To our surprise, the ether-based electrolyte-induced SEI coating on the Li-metal anode was implantable and worked well in a carbonate ester-based electrolyte.

The cells with both COM and advanced anodes realized a high discharge capacity (230  $\text{mAh g}^{-1}$ ) at 0.1 C (1.0 C = 182  $\text{mA g}^{-1}$ ) (Figure 5A). However, the coulombic efficiency decayed sharply from 97% to 82% in the COM cell, whereas 99% of the coulombic efficiency was maintained in the advanced cell. The advanced Li-metal anode showed many advantages when the current was increased to 182  $\text{mA g}^{-1}$  (Figures 5B and 5C). The COM cell failed at a large current as a result of its sluggish dynamics. Even after necessary activation at 18.2  $\text{mA g}^{-1}$ , the COM cell had a low capacity of 100  $\text{mAh g}^{-1}$ . In contrast, the advanced cell worked well at a large current of 182  $\text{mA g}^{-1}$  without any activation. The advanced cell displayed a very high capacity of 152  $\text{mAh g}^{-1}$ .

We observed the surface morphology by recording the COM and advanced anodes after 20 cycles at 182  $\text{mA g}^{-1}$ . Large dendrites, 10  $\mu\text{m}$  in diameter and more than 50  $\mu\text{m}$  in length, were found on the surface of the COM anode, whereas the surface of the advanced anode was quite smooth (Figure 5D). The cross-section morphology was also recorded after 20 cycles (Figure S7). The SEI layer in the COM and advanced anodes did not become too thick. However, the highly resistive reactive Li layer in the COM anode was much thicker than that in the advanced anode. Consequently,

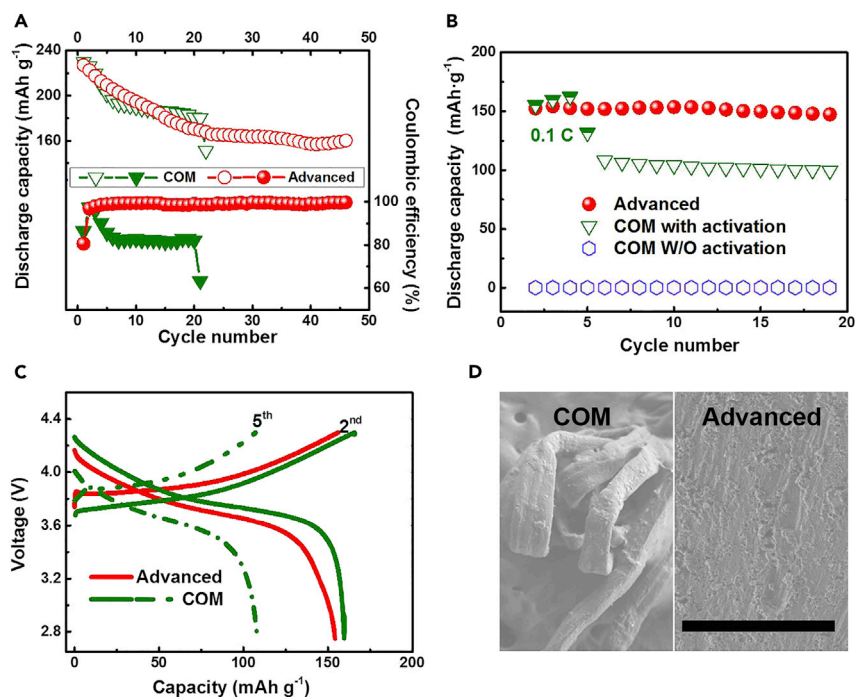


**Figure 5. Electrochemical Performance of Cells by Matching the Advanced Li-Metal Anode with an NCM Cathode**

(A and B) Cycling performance of cells tested at (A)  $18.2 \text{ mA g}^{-1}$  and (B)  $182 \text{ mA g}^{-1}$ .

(C) Charge and discharge curves of cells cycled at  $182 \text{ mA g}^{-1}$ .

(D) SEM images of the surface morphology of the COM and advanced Li-metal anodes after 20 cycles at  $182 \text{ mA g}^{-1}$ . The scale bar represents  $50 \mu\text{m}$ .

the ether-based-electrolyte-induced SEI coating on the Li-metal anode not only preserves its Li-dendrite-inhibiting behavior but also significantly enhances its high rate performance when matched with a NCM cathode.

## DISCUSSION

The high efficiency of the implantable SEI layer can be attributed to LiF species and the balanced co-existence of  $\text{Li}_2\text{S}$  and  $\text{Li}_2\text{S}_x\text{O}_y$  in the protective film. These species render a highly functional SEI layer with superior ionic conductivity and electrical insulation,<sup>40–42</sup> which is believed to be critically important for a safe LMB with high energy and power density. However, the formation of LiF is kinetically laborious because of the difficulty in breaking the bond of  $-\text{CF}_3$  in LiTFSI, although LiF is thermodynamically stable (Figure S2).<sup>41</sup> When LiPS is introduced into the precursor electrolyte, the highly reactive  $\text{Li}_2\text{S}_x\text{O}_y$ , attributed from the reaction between LiPS and  $\text{LiNO}_3$ , can promote the conversion from  $-\text{CF}_3$  to LiF (Figure S8). Along with other components, LiF renders a robust SEI film on the Li-metal anode. High-resolution TEM images of the  $\text{Li}_2\text{S}_5$ -induced implantable SEI film show a clearly polycrystalline structure with a uniform distribution of  $\text{Li}_3\text{N}$ ,  $\text{Li}_2\text{O}$ , LiF,  $\text{Li}_2\text{S}$ , and  $\text{Li}_2\text{SO}_4$  in the SEI film (Figure S9). These small crystals with balanced multi-components are very significant for a dense SEI film with high Li-ion conductivity.

In addition to  $\text{Li}_2\text{S}_5$  other LiPSs ( $\text{Li}_2\text{S}_x$ ,  $x = 1\text{--}8$ ) can act in a similar way to afford  $\text{Li}_2\text{S}_x\text{O}_y$  species to promote the generation of LiF (Figure S10). It seems that  $\text{Li}_2\text{S}_4$ ,  $\text{Li}_2\text{S}_5$ ,  $\text{Li}_2\text{S}_7$ , and  $\text{Li}_2\text{S}_8$  can achieve a superior performance in promoting the

conversion from  $-\text{CF}_3$  to LiF than  $\text{Li}_2\text{S}$ ,  $\text{Li}_2\text{S}_2$ ,  $\text{Li}_2\text{S}_3$ , or  $\text{Li}_2\text{S}_6$  at a sulfur concentration of 0.10 M. This phenomenon is attributed to the difference in the stability of the solution and the redox state of different Li polysulfides. However, elaborate experiments are required to clearly investigate the difference between them.

In this study, an implantable SEI was successfully electroplated on the surface of Li metal. An electroplated SEI induced by a LiTFSI (1.0 M)- $\text{LiNO}_3$  (5.0 wt %)- $\text{Li}_2\text{S}_5$  (0.02 M)-based-electrolyte was homogeneously distributed on the surface of Li metal to prevent immediate reactions between the Li metal and electrolyte. In terms of stability, robustness,  $\text{Li}^+$  transport properties, conformality, and so on, other ex situ (or artificial) SEIs with only one foreign material cannot satisfy the demand for a real SEI film with the complexity in structure and composition to meet the multiple requirements of working cells. The implantable SEI is an actual SEI formed ex situ on the Li-metal anode from an electrochemical cell, whereas the actual working cell does not need electrolyte additives to form the protective SEI. The potential negative effect of these electrolyte additives is therefore avoided, broadening the choices when constructing an implantable SEI. Thus, it is expected that implantable SEIs can protect Li metal synergistically and adaptively.

The advanced SEI increased the short-circuit time by 83% (from 3 to 5.5 hr) to suppress Li dendrite growth. Li-S pouch cells with the advanced Li-metal anode showed improved discharge capacity from 156 to 917  $\text{mAh g}^{-1}$  and enhanced coulombic efficiency from 12% to 85% at 0.1 C by protecting Li metal and inhibiting the shuttle of Li polysulfide intermediates. The electroplated implantable SEI could be extended to match a NCM cathode in carbonate ester-based electrolyte. At a low rate of 18.2  $\text{mA g}^{-1}$ , the COM cell showed a severe decay in coulombic efficiency from 97% to 82%, whereas the advanced cell maintained 99% stability. The superb high rate performance of the advanced Li-metal cell without any activation confirms the highly conductive nature of electroplated SEIs. This is the first time that a Li-metal anode formed in ether-based electrolyte has been applied to a carbonate ester-based electrolyte and has shown superior performance in dendrite-inhibiting behavior and cycling performance. The electroplated implantable SEI described here not only provides a creative method of constructing stable protection for a Li-metal anode but also makes it possible to obtain a Li-metal anode by compatibly coupling the superiority of SEIs formed in different electrolytes. The highly conductive and stable implantable SEI on the Li-metal anode represents a new branch of interfacial chemistry and a material platform for advanced energy storage systems with metal electrodes.

## EXPERIMENTAL PROCEDURES

### Materials

Li metal was obtained commercially from China Energy Lithium. The carbonate ester-based electrolyte of 1.0 M  $\text{LiPF}_6$ , dissolved in EC and DEC in a volumetric ratio of 1:1, and the ether-based electrolyte composed of LiTFSI (1.0 M), dissolved in DOL/DME in a volumetric ratio of 1:1, were purchased from the Beijing Chemical Industry Group. S,  $\text{Li}_2\text{S}$ , and  $\text{LiNO}_3$  powders were purchased from Alfa Aesar. The NCM cathode was provided by Huanyu Corporation. Multi-walled carbon nanotubes (MWCNTs) were produced by chemical vapor deposition on an Fe-based catalyst in a fluidized bed reactor, and routine purification by acid was carried out.

### Preparation of the Sulfur Cathode

The preparation of the sulfur cathode is described in our previous publication.<sup>46</sup> MWCNTs were mixed with sulfur powder and co-heated at 155°C in a sealed quartz bottle to yield the composites with 63 wt % sulfur. Polyvinylidene fluoride dissolved

in *N*-methyl-2-pyrrolidone was used as a binder to bind the MWCNT and sulfur composites onto an aluminum foil current collector with a blade thickness of 100  $\mu\text{m}$ . The film was then dried at 60°C for 6.0 hr. A sulfur loading of 1.1  $\text{mg cm}^{-2}$  on the electrode was obtained. Disks 13 mm in diameter were punched as the working cathodes for Li-S coin cells. The same method was used to fabricate sulfur cathodes for pouch cells, but the sulfur loading was improved to 4.43  $\text{mg cm}^{-2}$  and the total sulfur mass was 66.45 mg in pouch cells.

### Preparation of the Electroplated SEI on Li Metal

$\text{LiNO}_3$  was added to the LiTFSI-DOL/DME electrolyte to yield 5.0 wt %  $\text{LiNO}_3$  electrolyte. Advanced electrolyte with a  $\text{Li}_2\text{S}_5$  concentration of 0.02 M was obtained by the stoichiometric addition of  $\text{Li}_2\text{S}$  and S into the 5.0 wt %  $\text{LiNO}_3$  electrolyte. CR2025 Li and Li symmetrical cells with advanced electrolyte were assembled, charged, and then discharged in one cycle to form the ex situ electroplated SEI on Li metal. The discharge time was set at 1 hr with a cutoff voltage of  $-0.5\text{ V}$  at  $1.0\text{ mA cm}^{-2}$ , whereas the charge cutoff voltage was 0.5 V with the same current density. After one cycle, the coin cell was disassembled. The Li metal with the electroplated SEI was washed with DME solvent for the removal of Li salt. The washing process was carried out in a glove box with extra care. In addition, for preventing interference from pressure during preformation of the implantable SEI, the COM Li anode was also fabricated under the same pressure ( $50\text{ kg cm}^{-2}$ ) before the electrochemical measurements.

### Electrochemical Test

In a conventional coin cell, the pressure exerted by polymer separator,<sup>47</sup> pore structure,<sup>48</sup> and thermal conductivity<sup>49</sup> of the separator can seriously affect Li deposition behavior. For eliminating the interference of the separator and preserving the anode surface morphology after disassembly of the test cell, a hard Teflon circle was used as a spacer between the two electrodes.<sup>14,26,50</sup> STC24 dismountable cells (MTI Corporation) were specially customized for detection of the short-circuit time with the circinate Teflon separator (0.5 mm in thickness, 16 mm in outer diameter, and 13 mm in inner diameter) instead of Celgard 2400 in a battery. Li-S coin and pouch cells were assembled with a sulfur cathode, Celgard 2400 separator, and COM/advanced in the LiTFSI-DOL/DME electrolyte. The Li-S cells were operated in a voltage window of 1.8–2.8 V. The COM and advanced anodes were also matched with a  $\text{LiNi}_{0.5}\text{Co}_{0.2}\text{Mn}_{0.3}\text{O}_2$  cathode (loading = 12.02  $\text{mg cm}^{-2}$ ) in a coin cell with a  $\text{LiPF}_6\text{-EC/DEC}$  electrolyte. The NCM cathode cells were operated in a voltage window of 2.8–4.3 V. All cells were assembled and separated in a glove box filled with Ar with  $\text{O}_2$  and  $\text{H}_2\text{O}$  content below 1.0 ppm.

### Material Characterization

The morphology of Li metal was examined with a JSM 7401F scanning electron microscope operated at 3.0 kV and a JEM 2100 transmission electron microscope operated at 120.0 kV. XPS was used with Al-K  $\alpha$  radiation (72 W and 12 kV) at a pressure of  $10^{-9}$  Torr. The diameter of area analyzed was 400  $\mu\text{m}$ . A time-of-flight secondary ion mass spectrometer (TOF.SIMS 5, ION-TOF) at a pressure below  $10^{-9}$  Torr was used for cross-section mapping and analysis of the depth of the chemical composition of Li-metal anodes. A  $\text{Bi}^{3+}$  (30 keV, 3 pA) ion beam was used as the primary source for detecting the composition of cross-section Li mapping, and the analysis area was  $500 \times 500\ \mu\text{m}^2$ . Sputtering with a  $\text{Cs}^+$  ion beam (2 keV, 70 nA) was used for depth profiling analysis. The sputtering rate of Li by the  $\text{Cs}^+$  beam was estimated to be  $\sim 0.68\text{ nm s}^{-1}$ . The sputtering time was 3,000 s for a depth of 2  $\mu\text{m}$  with a sputtering area of  $500 \times 500\ \mu\text{m}^2$ . For avoiding oxidation and parasitical reactions before transfer to the test chamber, the sample was prepared in a

glove box and placed into a home made container. In situ optical microscopy was used to investigate Li deposition behavior and changes in the morphology of the advanced Li anode. A quartz cell with transparent windows was used as the electrode housing, in which a symmetrical cell with advanced and COM electrodes was assembled (without a conventional polymer separator). The electrode area of advanced and COM Li electrodes was  $0.15 \text{ cm}^{-2}$ . The distance between the Li and COM Li electrodes was approximately 0.7 cm. The applied current and each electroplating and electrostripping time were set to 10 mA and 100 s, respectively.

### Calculation of HOMO and LUMO Energy

All calculations were performed in the Gaussian 09 program with the density functional theory method.<sup>51</sup> The B3LYP hybrid function<sup>52</sup> and 6-311G++ (d, p) basis were adopted. The force constant was calculated once, and the frequency was calculated to confirm the structure. A default spin was adopted during the calculation. For testing the stability of specific components, molecules with charge were also considered.

### SUPPLEMENTAL INFORMATION

Supplemental Information includes ten figures and can be found with this article online at <http://dx.doi.org/10.1016/j.chempr.2017.01.003>.

### AUTHOR CONTRIBUTIONS

Q.Z. conceived and designed this work; Q.Z., X.-B.C., and C.Y. designed all experiments; X.-B.C. fabricated the Li-metal anode with the implantable SEI; C.Y. measured the cell performance; X.C. calculated the HOMO and LUMO levels; C.G. conducted the in situ optical observation of Li dendrite growth; J.H., R.Z., and H.P. performed characterization of the Li metal with the implantable SEI; X.-B.C. and Q.Z. wrote the paper; all authors participated in the analysis of the experimental data and discussions of the results, as well as preparation of the paper.

### ACKNOWLEDGMENTS

This work was supported by the National Key Research and Development Program (2016YFA0202500 and 2015CB932500), the Natural Scientific Foundation of China (21422604, 21676160, and 21561130151), and the Tsinghua National Laboratory for Information Science and Technology.

Received: August 30, 2016

Revised: September 26, 2016

Accepted: January 5, 2017

Published: February 9, 2017

### REFERENCES AND NOTES

1. Tarascon, J.M., and Armand, M. (2001). Issues and challenges facing rechargeable lithium batteries. *Nature* 414, 359–367.
2. Ottakam Thotiyl, M.M., Freunberger, S.A., Peng, Z., Chen, Y., Liu, Z., and Bruce, P.G. (2013). A stable cathode for the aprotic Li-O<sub>2</sub> battery. *Nat. Mater.* 12, 1050–1056.
3. Armand, M., and Tarascon, J.M. (2008). Building better batteries. *Nature* 451, 652–657.
4. Kim, H., Jeong, G., Kim, Y.U., Kim, J.H., Park, C.M., and Sohn, H.J. (2013). Metallic anodes for next generation secondary batteries. *Chem. Soc. Rev.* 42, 9011–9034.
5. Xu, W., Wang, J., Ding, F., Chen, X., Nasybulin, E., Zhang, Y., and Zhang, J.-G. (2014). Lithium metal anodes for rechargeable batteries. *Energy Environ. Sci.* 7, 513–537.
6. Park, M.S., Ma, S.B., Lee, D.J., Im, D., Doo, S.G., and Yamamoto, O. (2014). A highly reversible lithium metal anode. *Sci. Rep.* 4, 3815.
7. Cheng, X.-B., Zhang, R., Zhao, C.-Z., Wei, F., Zhang, J.-G., and Zhang, Q. (2016). A review of solid electrolyte interphases on lithium metal anode. *Adv. Sci. (Weinh)* 3, 1500213.
8. Sun, Y., Liu, N., and Cui, Y. (2016). Promises and challenges of nanomaterials for lithium-based rechargeable batteries. *Nat. Energy* 1, 16071.
9. Busche, M.R., Drossel, T., Leichtweiss, T., Weber, D.A., Falk, M., Schneider, M., Reich, M.L., Sommer, H., Adelhelm, P., and Janek, J. (2016). Dynamic formation of a solid-liquid electrolyte interphase and its consequences for hybrid-battery concepts. *Nat. Chem.* 8, 426–434.
10. Xu, K. (2014). Electrolytes and interphases in Li-ion batteries and beyond. *Chem. Rev.* 114, 11503–11618.
11. Gauthier, M., Carney, T.J., Grimaud, A., Giordano, L., Pour, N., Chang, H.-H., Fenning,

- D.P., Lux, S.F., Paschos, O., Bauer, C., et al. (2015). Electrode-electrolyte interface in Li-ion batteries: current understanding and new insights. *J. Phys. Chem. Lett.* **6**, 4653–4672.
12. Gireaud, L., Grugeon, S., Laruelle, S., Yrieix, B., and Tarascon, J.M. (2006). Lithium metal stripping/plating mechanisms studies: a metallurgical approach. *Electrochem. Commun.* **8**, 1639–1649.
13. Zu, C., Dolocan, A., Xiao, P., Stauffer, S., Henkelman, G., and Manthiram, A. (2016). Breaking down the crystallinity: the path for advanced lithium batteries. *Adv. Energy Mater.* **6**, 1501933.
14. Lu, Y., Tu, Z., and Archer, L.A. (2014). Stable lithium electrodeposition in liquid and nanoporous solid electrolytes. *Nat. Mater.* **13**, 961–969.
15. Ozhabes, Y., Gunceler, D., and Arias, T.A. (2015). Stability and surface diffusion at lithium-electrolyte interphases with connections to dendrite suppression. *arXiv*, 1504.05799.
16. Tu, Z., Nath, P., Lu, Y., Tikekar, M.D., and Archer, L.A. (2015). Nanostructured electrolytes for stable lithium electrodeposition in secondary batteries. *Acc. Chem. Res.* **48**, 2947–2956.
17. Lu, Y., Tikekar, M., Mohanty, R., Hendrickson, K., Ma, L., and Archer, L.A. (2015). Stable cycling of lithium metal batteries using high transference number electrolytes. *Adv. Energy Mater.* **5**, 1402073.
18. Zhou, D., Liu, R., He, Y.-B., Li, F., Liu, M., Li, B., Yang, Q.-H., Cai, Q., and Kang, F. (2016). SiO<sub>2</sub> hollow nanosphere-based composite solid electrolyte for lithium metal batteries to suppress lithium dendrite growth and enhance cycle life. *Adv. Energy Mater.* **6**, 1502214.
19. Qian, J., Henderson, W.A., Xu, W., Bhattacharya, P., Engelhard, M., Borodin, O., and Zhang, J.G. (2015). High rate and stable cycling of lithium metal anode. *Nat. Commun.* **6**, 6362.
20. Suo, L., Hu, Y.S., Li, H., Armand, M., and Chen, L. (2013). A new class of solvent-in-salt electrolyte for high-energy rechargeable metallic lithium batteries. *Nat. Commun.* **4**, 1481.
21. Yamada, Y., and Yamada, A. (2015). Review—superconcentrated electrolytes for lithium batteries. *J. Electrochem. Soc.* **162**, A2406–A2423.
22. Suo, L., Borodin, O., Gao, T., Olguin, M., Ho, J., Fan, X., Luo, C., Wang, C., and Xu, K. (2015). “Water-in-salt” electrolyte enables high-voltage aqueous lithium-ion chemistries. *Science* **350**, 938–943.
23. Ding, F., Xu, W., Graff, G.L., Zhang, J., Sushko, M.L., Chen, X., Shao, Y., Engelhard, M.H., Nie, Z., Xiao, J., et al. (2013). Dendrite-free lithium deposition via self-healing electrostatic shield mechanism. *J. Am. Chem. Soc.* **135**, 4450–4456.
24. Liu, Q.C., Xu, J.J., Yuan, S., Chang, Z.W., Xu, D., Yin, Y.B., Li, L., Zhong, H.X., Jiang, Y.S., Yan, J.M., et al. (2015). Artificial protection film on lithium metal anode toward long-cycle-life lithium-oxygen batteries. *Adv. Mater.* **27**, 5241–5247.
25. Heine, J., Krüger, S., Hartnig, C., Wietelmann, U., Winter, M., and Bieker, P. (2014). Coated lithium powder (CLiP) electrodes for lithium-metal batteries. *Adv. Energy Mater.* **4**, 1300815.
26. Cheng, X.B., Peng, H.J., Huang, J.Q., Zhang, R., Zhao, C.Z., and Zhang, Q. (2015). Dual-phase lithium metal anode containing a polysulfide-induced solid electrolyte interphase and nanostructured graphene framework for lithium-sulfur batteries. *ACS Nano* **9**, 6373–6382.
27. Zhang, R., Cheng, X.-B., Zhao, C.-Z., Peng, H.-J., Shi, J.-L., Huang, J.-Q., Wang, J., Wei, F., and Zhang, Q. (2016). Conductive nanostructured scaffolds render low local current density to inhibit lithium dendrite growth. *Adv. Mater.* **28**, 2155–2162.
28. Sun, Y., Zheng, G., Seh, Z.W., Liu, N., Wang, S., Sun, J., Lee, H.R., and Cui, Y. (2016). Graphite-encapsulated Li-metal hybrid anodes for high-capacity Li batteries. *Chem* **1**, 287–297.
29. Cheng, X.B., Peng, H.J., Huang, J.Q., Wei, F., and Zhang, Q. (2014). Dendrite-free nanostructured anode: entrapment of lithium in a 3D fibrous matrix for ultra-stable lithium-sulfur batteries. *Small* **10**, 4257–4263.
30. Yang, C.P., Yin, Y.X., Zhang, S.F., Li, N.W., and Guo, Y.G. (2015). Accommodating lithium into 3D current collectors with a submicron skeleton towards long-life lithium metal anodes. *Nat. Commun.* **6**, 8058.
31. Lu, L.-L., Ge, J., Yang, J.-N., Chen, S.-M., Yao, H., Zhou, F., and Yu, S.-H. (2016). Free-standing copper nanowire network current collector for improving lithium anode performance. *Nano Lett.* **16**, 4431–4437.
32. Yun, Q., He, Y.-B., Lv, W., Zhao, Y., Li, B., Kang, F., and Yang, Q.-H. (2016). Chemical dealloying derived 3D porous current collector for Li metal anodes. *Adv. Mater.* **28**, 6932–6939.
33. Huang, C., Xiao, J., Shao, Y., Zheng, J., Bennett, W.D., Lu, D., Saraf, L.V., Engelhard, M., Ji, L., Zhang, J., et al. (2014). Manipulating surface reactions in lithium-sulphur batteries using hybrid anode structures. *Nat. Commun.* **5**, 3015.
34. Cheng, X.-B., Hou, T.-Z., Zhang, R., Peng, H.-J., Zhao, C.-Z., Huang, J.-Q., and Zhang, Q. (2016). Dendrite-free lithium deposition induced by uniformly distributed lithium ions for efficient lithium metal batteries. *Adv. Mater.* **28**, 2888–2895.
35. Liang, Z., Zheng, G., Liu, C., Liu, N., Li, W., Yan, K., Yao, H., Hsu, P.-C., Chu, S., and Cui, Y. (2015). Polymer nanofiber-guided uniform lithium deposition for battery electrodes. *Nano Lett.* **15**, 2910–2916.
36. Chu, S., and Cui, Y. (2016). Selective deposition and stable encapsulation of lithium through heterogeneous seeded growth. *Nat. Energy* **1**, 16010.
37. Zheng, G., Lee, S.W., Liang, Z., Lee, H.W., Yan, K., Yao, H., Wang, H., Li, W., Chu, S., and Cui, Y. (2014). Interconnected hollow carbon nanospheres for stable lithium metal anodes. *Nat. Nanotechnol.* **9**, 618–623.
38. Li, N.W., Yin, Y.X., Yang, C.P., and Guo, Y.G. (2016). An artificial solid electrolyte interphase layer for stable lithium metal anodes. *Adv. Mater.* **28**, 1853–1858.
39. Zhao, C.-Z., Cheng, X.-B., Zhang, R., Peng, H.-J., Huang, J.-Q., Ran, R., Huang, Z.-H., Wei, F., and Zhang, Q. (2016). Li<sub>2</sub>S<sub>5</sub>-based ternary-salt electrolyte for robust lithium metal anode. *Energy Storage Mater.* **3**, 77–84.
40. Xiong, S., Xie, K., Diao, Y., and Hong, X. (2014). Characterization of the solid electrolyte interphase on lithium anode for preventing the shuttle mechanism in lithium-sulfur batteries. *J. Power Sources* **246**, 840–845.
41. Li, W., Yao, H., Yan, K., Zheng, G., Liang, Z., Chiang, Y.M., and Cui, Y. (2015). The synergistic effect of lithium polysulfide and lithium nitrate to prevent lithium dendrite growth. *Nat. Commun.* **6**, 7436.
42. Pan, J., Cheng, Y.-T., and Qi, Y. (2015). General method to predict voltage-dependent ionic conduction in a solid electrolyte coating on electrodes. *Phys. Rev. B* **91**, 134116.
43. Ji, X., Lee, K.T., and Nazar, L.F. (2009). A highly ordered nanostructured carbon-sulphur cathode for lithium-sulphur batteries. *Nat. Mater.* **8**, 500–506.
44. Yabuuchi, N., and Ohzuku, T. (2003). Novel lithium insertion material of LiCo<sub>1/3</sub>Ni<sub>1/3</sub>Mn<sub>1/3</sub>O<sub>2</sub> for advanced lithium-ion batteries. *J. Power Sourc.* **119–121**, 171–174.
45. Jung, S.-K., Gwon, H., Hong, J., Park, K.-Y., Seo, D.-H., Kim, H., Hyun, J., Yang, W., and Kang, K. (2014). Understanding the degradation mechanisms of LiNi<sub>0.5</sub>Co<sub>0.2</sub>Mn<sub>0.3</sub>O<sub>2</sub> cathode material in lithium ion batteries. *Adv. Energy Mater.* **4**, 1300787.
46. Cheng, X.-B., Huang, J.-Q., Zhang, Q., Peng, H.-J., Zhao, M.-Q., and Wei, F. (2014). Aligned carbon nanotube/sulfur composite cathodes with high sulfur content for lithium-sulfur batteries. *Nano Energy* **4**, 65–72.
47. Ferrese, A., and Newman, J. (2014). Mechanical deformation of a lithium-metal anode due to a very stiff separator. *J. Electrochem. Soc.* **161**, A1350–A1359.
48. Shin, W.-K., Kannan, A.G., and Kim, D.-W. (2015). Effective suppression of dendritic lithium growth using an ultrathin coating of nitrogen and sulfur codoped graphene nanosheets on polymer separator for lithium metal batteries. *ACS Appl. Mater. Inter.* **7**, 23700–23707.
49. Luo, W., Zhou, L., Fu, K., Yang, Z., Wan, J., Manno, M., Yao, Y., Zhu, H., Yang, B., and Hu, L. (2015). A thermally conductive separator for stable Li metal anodes. *Nano Lett.* **15**, 6149–6154.
50. Hendrickson, K.E., Ma, L., Cohn, G., Lu, Y., and Archer, L.A. (2015). Model membrane-free Li-S batteries for enhanced performance and cycle life. *Adv. Sci. (Weinh)* **2**, 1500068.
51. Hohenberg, P., and Kohn, W. (1964). Inhomogeneous electron gas. *Phys. Rev.* **136**, B864–B871.
52. Becke, A.D. (1993). Density-functional thermochemistry. III. The role of exact exchange. *J. Chem. Phys.* **98**, 5648–5652.